

Article

Design and Performance Evaluation of an Enclosed Inertial Wave Energy Converter with a Nonlinear Stiffness Mechanism

Jian Qin ¹, Zhenquan Zhang ¹, Xuening Song ¹, Shuting Huang ¹, Yanjun Liu ^{1,2,*}  and Gang Xue ^{1,2,*} 

¹ Institute of Marine Science and Technology, Shandong University, Qingdao 266237, China; 201916191@mail.sdu.edu.cn (J.Q.); zh_zhenquan@mail.sdu.edu.cn (Z.Z.); 202336925@mail.sdu.edu.cn (X.S.); hst@sdu.edu.cn (S.H.)

² School of Mechanical Engineering, Key Laboratory of High-Efficiency and Clean Mechanical Manufacture, Ministry of Education, National Demonstration Center for Experimental Mechanical Engineering Education, Shandong University, Jinan 250061, China

* Correspondence: lyj111@sdu.edu.cn (Y.L.); xuegang@sdu.edu.cn (G.X.); Tel.: +86-0532-58633267 (Y.L.)

† These authors contributed equally to this work.

Abstract: In order to enhance the power generation efficiency and reliability of wave energy converters (WECs), an enclosed inertial WEC with a magnetic nonlinear stiffness mechanism (nonlinear EIWEC) is proposed in this paper. A mathematical model of the nonlinear EIWEC was established based on the Cummins equation and the equivalent magnetic charge method, and the joint simulations were carried out using MATLAB/Simulink 2020 and AMESim 2020 softwares. The effect of the magnetic nonlinear stiffness mechanism (NSM) on the performance of the EIWEC system was investigated. The results show that the nonlinear negative stiffness property of NSM can significantly improve the motion response and output power of EIWEC under low-frequency waves. Compared to EIWEC without NSM (linear EIWEC), nonlinear EIWEC has a higher generation efficiency and wider frequency bandwidth. Additionally, the effects of linear spring, internal mass body, and hydraulic power take-off (PTO) system parameters on the energy conversion capability of the system were analyzed to provide a reference for the design of nonlinear EIWECs. In general, the proposed nonlinear EIWEC could provide good development potential for the scale utilization of wave energy resources.

Keywords: wave energy converter; nonlinear stiffness mechanism; hydraulic PTO system; wide bandwidth; AMESim



Citation: Qin, J.; Zhang, Z.; Song, X.; Huang, S.; Liu, Y.; Xue, G. Design and Performance Evaluation of an Enclosed Inertial Wave Energy Converter with a Nonlinear Stiffness Mechanism. *J. Mar. Sci. Eng.* **2024**, *12*, 191. <https://doi.org/10.3390/jmse12010191>

Academic Editor: Barbara Zanuttigh

Received: 16 December 2023

Revised: 15 January 2024

Accepted: 18 January 2024

Published: 20 January 2024



Copyright: © 2024 by the authors. Licensee MDPI, Basel, Switzerland. This article is an open access article distributed under the terms and conditions of the Creative Commons Attribution (CC BY) license (<https://creativecommons.org/licenses/by/4.0/>).

1. Introduction

With the rapid expansion of the global economy and population, the energy crisis and climate change have reached a heightened level of urgency [1]. Various measures have been implemented, including the United Nations Framework Convention on Climate Change [2] and the Paris Agreement [3], aimed at mitigating the impact of global warming and fostering sustainable development across economic, social, and environmental domains. There is now a widespread consensus among the international community to change the conventional fossil-fuel-based energy structure and actively advance the utilization of renewable energy resources [4,5].

The oceans encompass 71% of the Earth's surface and are abundant in energy resources [6]. Wave energy, one of the typical ocean energy resources, has advantages such as better availability, greater predictability, and higher energy density [7]. Wave energy can provide electricity support for island communities, ocean observation instruments, aquaculture activities [8,9], and hydrogen production and desalination [10], exhibiting vast application potential.

In recent years, many wave energy converters (WECs) have been proposed, such as oscillating buoy WECs, oscillating water column WECs, and overtopping WECs [11]. These diverse design concepts have contributed to effectively developing and utilizing wave

energy resources. However, the diversity of concepts is also detrimental, in the sense that there is no “winning concept” at this moment. This hinders potential economies of scale and standardization gains, as well as diluting the investments made into wave energy. Moreover, in these concepts, almost all of the WEC’s units, such as the power take-off (PTO) system, control system, and electrical system, are directly exposed to the marine environment. The entire WEC will be affected by all processes: biofouling, corrosion, extreme waves, etc. [12] These elements of the marine environment can make critical units (especially the PTO system) less reliable. These situations can increase the LCOE, either through lower efficiency, higher downtimes or greater expenditures in operation and maintenance.

Enclosed inertial WECs (EIWECs) have attracted much attention from scholars because of their outstanding survivability and reliable working performance [13]. Prominent EIWECs include Searev [14], Pendulum WEC (PeWEC) [15], Inertial Sea WEC (ISWEC) [16], the Wello Oy Penguin [17], the E-Motions [18], the Seaturms [19] and the WITT [20], and their survivability has generally been verified under extreme wave scenarios. They feature the enclosure of every PTO component inside a rigid and watertight buoy. The encapsulation structure protects all the internal parts from potential risks of corrosion or flooding [21]. Under wave excitation, energy harvesting is achieved by relative motion (linear or rotational motion) between the buoy and the internal mass body [16,22,23]. Therefore, this study will focus on performance analysis and optimization of the EIWECs.

Improving the generation efficiency of the WECs plays an essential role in reducing the LCOE. Efficient power extraction from the ocean in EIWECs with linear stiffness springs (linear EIWECs) is achievable when the system operates near resonance [24]. However, wave energy is primarily distributed within a period range from 5 s to 15 s, exhibiting broadband and low-frequency characteristics [25]. It is difficult for linear WECs to adequately harvest energy from the wide frequency band of the ocean waves, thereby leaving most of the wave energy unutilized [26]. The natural frequency of the WEC is determined by the stiffness of the hydrostatic force, which is typically very high, resulting in a natural frequency much higher than the dominant frequencies in the spectrum of the incoming ocean waves [27]. For instance, for a point absorber with a diameter of 4 m, its natural frequency is about 1.78 rad/s, which means that the system can resonate at a wave period of 3.5 s [28]. This value is considerably lower than the common wave period. To accommodate the low-frequency characteristics of ocean waves, larger-sized buoys are necessary to achieve reduced intrinsic frequencies of WECs [29]. According to Kurniawan et al. [29], to resonate at 8 s (typical Wave Period), a point absorber would need a diameter of approximately 30 m. However, the large-sized floats may pose additional challenges, including wave-structure interactions, economies of scale and costs. Moreover, these larger-sized floats might be less hydrodynamically efficient than smaller bodies due to opposing forces over the body surface [30].

Numerous techniques have been put forth to enhance efficiency, including modifying the mass moment of inertia and actively controlling the PTO system [21,31–33]. These methods typically involve real-time parameter tuning based on estimating the wave excitation force and are challenging to implement in practice [34]. The prediction deviation of wave information might cause a significant decrease in control performance. Furthermore, these control strategies required extra control units, inevitably increasing installation and maintenance expenses.

In the field of mechanical vibration energy harvesting, nonlinearities and instabilities are typically introduced into the system to increase frequency bandwidth and the dynamic range of the excitation amplitude. Scapolan [35] and Giorgi et al. [36] introduced a time-varying damper, tackling the problem of the performance enhancement of a mechanical energy harvester, in terms of both frequency bandwidth and response amplitude, via time variations of the PTO damping coefficient. Some WECs adopted parametric resonance to improve the energy conversion performance of the system. To meet the configuration requirements for parametric resonance, the float is usually connected to the pendulum for

inertial coupling in some schemes [37]. According to Giorgi [38], nonlinear hydrodynamics are also capable of inducing parametric resonance between different degrees of freedom of the float. In addition to the foregoing methods, the nonlinear stiffness approach, such as the bistable mechanism [39] and the collision mechanism [40], can also improve the frequency bandwidth and performance of the WECs. The bistable mechanism has two potential wells and a potential barrier, which can be obtained through the inclined structural configuration of springs or repulsive force between magnets [41,42]. For a bistable WEC system, there are three main motion patterns: periodic intrawell, interwell, and chaotic motion [43]. Among them, interwell motion can travel across the potential barrier and oscillate continuously between two potential wells, can generate a larger motion amplitude, and is considered to be a desirable high-energy orbit [28]. Recently, bistability has also been applied to EIWEC. Wang et al. [44] investigated the performance of a bistable snap-through PTO system operating inside a submerged EIWEC, highlighting the significance of the bistable mechanism in improving efficiency. Todalshaug et al. [45] proposed a bistable mechanism called “CorPower” and performed experiments on a 1/16-scale model. The results indicate that CorPower can provide phase control to the system, significantly increasing the power performance. The component was applied to the CorPower prototype [46]. Additionally, a novel X-shaped structure, offering an innovative bistable and quasi-zero stiffness, was applied in the EIWEC, thereby greatly enhancing the wave energy conversion capability [47]. These studies indicated that the utilization of nonlinear stiffness properties enables the passive tuning of the system. Nonlinear stiffness mechanisms are advantageous in adapting the system to wave frequency variations since the frequency bandwidth of the system is increased. However, this benefit is limited to large amplitude wave scenarios; when the wave height is small, the nonlinear stiffness may hinder the power extraction of EIWECs.

In our previous study, a novel magnetic nonlinear stiffness mechanism (NSM) was proposed and applied to a point absorber WEC (PAWEC) [28]. The NSM system exhibited a lower potential barrier, facilitating the buoyancy of PAWEC to generate high-energy interwell motions even in low amplitude waves. This characteristic significantly enhanced the energy harvesting efficiency and expanded the frequency bandwidth of the PAWEC. In this study, we extended the application of NSM in EIWEC (nonlinear EIWEC) and further assessed the influence of the nonlinear stiffness mechanism on the dynamics and power conversion performance of EIWEC.

Because of its great adaptability to low frequency waves and high efficiency, the hydraulic power take-off (PTO) system is a popular option for energy conversion in WECs [48]. Choi et al. [49] constructed and tested a 50 kW hydraulic PTO system, confirming the positive role of the accumulator in smoothing the power output. Gao et al. [50] considered the nonlinear effect of the hydraulic system and analyzed the influence of wave and hydraulic component parameters on motion response and performance. Liu et al. [51] employed the hydraulic PTO system to capture wave energy in a two-raft-type WEC. They discussed the variation in the optimal hydraulic PTO parameters with wave state. To improve the efficiency and stability of the rotating EIWEC, an adaptive hydraulic PTO system was designed and tested by Xue et al. [52]. The effects of the precharged pressure, delay time, and open state time of the accumulator on the average output power and power fluctuation index were experimentally analyzed.

The hydraulic PTO system typically consists of multiple hydraulic components, and variations in component parameters will result in complex energy conversion and force reaction characteristics [48]. To the authors’ knowledge, in the field of wave energy harvesting, few studies focused on the analysis and performance evaluation of hydraulic PTO systems coupled with nonlinear stiffness mechanisms. In previous studies of WECs with nonlinear stiffening mechanisms [28,39,40,43,53], the PTO system is frequently modeled as a linear relationship between the damping coefficient and the velocity. In this paper, the hydraulic PTO system was further introduced into the nonlinear EIWEC to ensure that the analysis more closely resembles a real scenario. However, the complex dynamic

behavior of the NSM will increase the design difficulty of the hydraulic PTO system. To address the issue, this paper investigated the effects of critical hydraulic PTO parameters on the performance of the nonlinear EIWEC system. The novelty of this paper is in two main aspects: (a) An enclosed inertial wave energy converter with a nonlinear stiffness mechanism was designed and proposed. The encapsulation structure can protect critical hydraulic PTO components from potential risks of corrosion or flooding. The nonlinear stiffness mechanism can increase the motion response and frequency bandwidth of the system, improving the operating performance of the EIWEC. (b) The hydraulic PTO system was further introduced into the nonlinear EIWEC. The results are expected to be a helpful reference for the hydraulic PTO system design of the nonlinear EIWEC.

The remainder of the paper is organized as follows. Section 2 describes the schematic design and models of the nonlinear EIWEC. In Section 3, the influence of nonlinear stiffness mechanisms and critical hydraulic PTO parameters on the motion response and performance of the system is discussed. Section 4 presents the main conclusions.

2. Schematic Design and Modeling

2.1. Schematic Design

The proposed enclosed inertial wave energy converter with a nonlinear stiffness mechanism (nonlinear EIWEC) is illustrated in Figure 1. As depicted in Figure 1a, the nonlinear EIWEC primarily consists of an energy harvester and a nonlinear stiffness mechanism (NSM), which are connected via a rod.

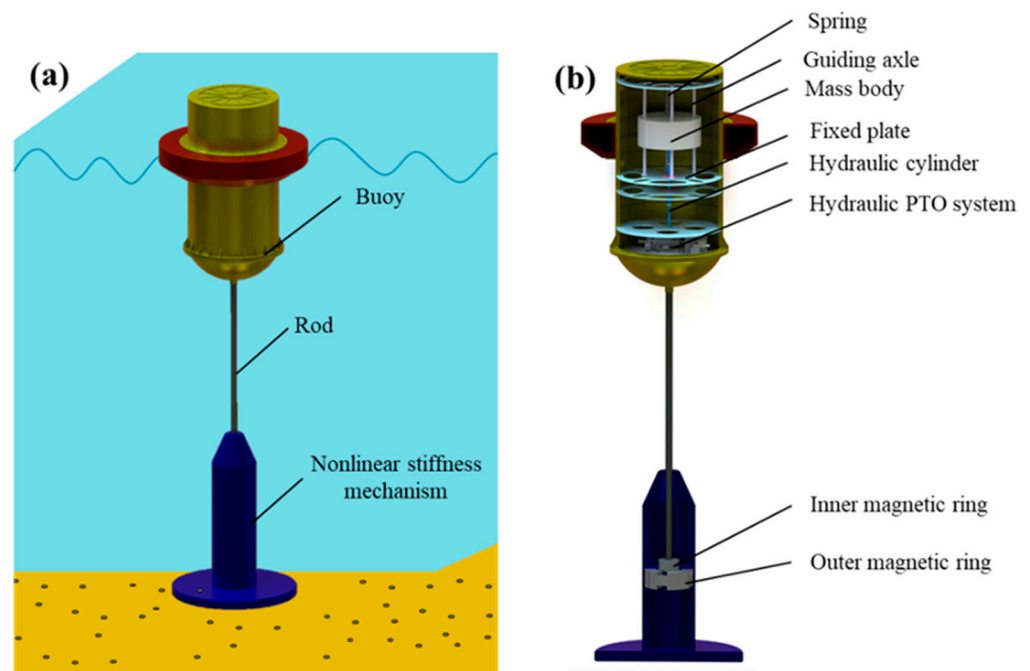


Figure 1. Nonlinear enclosed inertial wave energy converter (nonlinear EIWEC). (a) Working scenario, (b) internal structure.

Figure 1b shows a schematic diagram of the internal structure. The energy harvester comprises an inner mass body, a buoy, a linear spring, and a hydraulic PTO unit. These components are encapsulated inside a rigid and watertight buoy. The encapsulation structure can protect all the internal parts from potential risks of corrosion or flooding. The relative heaving motion between the buoy and the internal mass body can drive the hydraulic PTO system to generate electricity.

Figure 2 illustrates a working schematic of the nonlinear EIWEC. The buoy and inner mass body are connected by a linear spring that can transfer the wave energy captured by the buoy to the inner mass body. The cylinder and piston rod of the hydraulic cylinder

are mounted on the inner mass body and the buoy, respectively. Because of the relative motion between the inner mass body and the buoy, the upper and lower chambers of the hydraulic cylinder produce a pressure difference, allowing the oil to flow into the hydraulic PTO system (Figure 2a). Four check valves rectify the oil flow in the hydraulic motor into one direction. An accumulator is utilized to absorb flow fluctuations within the pipeline and stabilize the output speed of the hydraulic motor. After that, the oil flows into the hydraulic motor through the throttle valve. The hydraulic motor rotates and drives the generator to produce electrical energy.

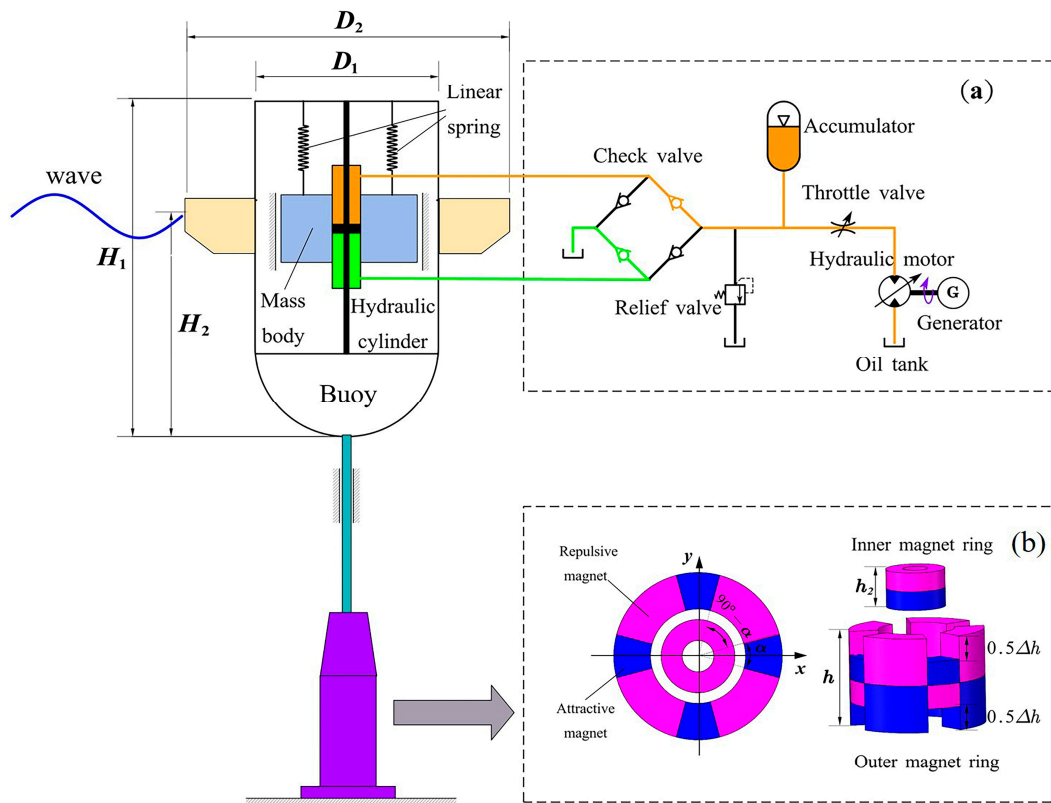


Figure 2. Working schematic of nonlinear EIWEC. (a) Hydraulic PTO unit, (b) nonlinear stiffness mechanism (NSM).

Figure 2b shows the three-dimensional structure of the NSM, and it comprises an inner and an outer magnetic ring. The inner magnetic ring is connected to the buoy via the rod, following the buoy to produce a heaving motion. The outer magnetic ring consists of two types of sector magnets with opposite magnetic poles and is mounted in the housing fixed to the seabed. The sector magnets with the same pole direction as the inner magnetic ring are ‘repulsive magnets’. The remaining sector magnets are ‘attractive magnets’ [28]. The primary role of the NSM is to provide nonlinear stiffness force to the buoy to increase the motion amplitude and improve the energy conversion performance of the EIWEC.

2.2. Mathematical Modeling

According to Guo et al. [40], under wave excitation, the buoy of a wave energy converter moves mainly in the heave direction. To simplify the model, we only consider the heaving motion response in terms of the structural design of the EIWEC. The nonlinear stiffness mechanism is mounted on the seabed, connected to the float by a rigid linkage. As a result, the buoy of the EIWEC can only generate a motion response in the heave degree of freedom.

As shown in Figure 3, the nonlinear EIWEC consists of three stiffness terms: hydrostatic stiffness k_{hs} , linear spring stiffness k , and magnetic nonlinear stiffness k_m . When

analyzing the effect of k_m on the system's performance, the effect of the other two stiffness terms should also be considered. The effects of k_m and k on the motion response of the EIWEC are evaluated in this section since k_{hs} is a constant term.

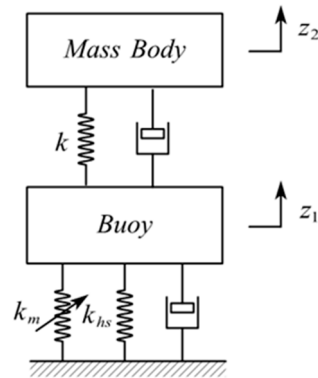


Figure 3. Vibration model of a nonlinear EIWEC.

The buoy is mainly subjected to wave excitation force F_e , radiation force F_r , hydrostatic restoring force F_{hs} , axial magnetic force of NSM F_m , and interaction force between the buoy and the mass body F_i . The dynamic model of the nonlinear EIWEC can be expressed as follows:

$$m_1 \ddot{z}_1 = F_e + F_r + F_{hs} + F_m + F_i, \tag{1}$$

where m_1 denotes the mass of the buoy, and \ddot{z}_1 is the acceleration of the buoy in the heave direction.

The equations of motion of the internal mass body are as follows:

$$m_2 \ddot{z}_2 = -F_i, \tag{2}$$

where m_2 denotes the mass of the mass body and \ddot{z}_2 is the heave acceleration of the mass body. The interaction force F_i depends on the relative motion between the buoy and the mass body and can be written as

$$F_i = k(z_2 - z_1) + F_{PTO}, \tag{3}$$

where k denotes the stiffness coefficient of the linear spring and F_{PTO} denotes the reaction force of the hydraulic PTO system. z_1 and z_2 represent the displacements of the buoy and the mass body, respectively. $z_3 = z_2 - z_1$, z_3 represents the relative displacement between the inner mass body and the buoy.

In addition, considering the limited internal space of the buoy, we use the initial elongation Δl instead of the spring stiffness k to avoid choosing some impractical stiffness.

$$\Delta l = \frac{m_2 g}{k}, \tag{4}$$

In regular waves, the wave excitation force F_e acting on a buoy can be expressed through the Haskind relation as [54]:

$$F_e = A \sqrt{\frac{2g^3 \rho B_z(\omega)}{\omega^3}} \cos(\omega t + \varphi), \tag{5}$$

where A is the amplitude of the wave, ρ is the density of seawater, g is the acceleration of gravity, $B_z(\omega)$ is the radiation damping coefficient, ω is the frequency of the wave, and φ is the phase of the wave.

According to the Cummins equation [55], the wave radiation force F_r can be given as

$$F_r = -m_\infty \ddot{z}_1 - \int_0^t k_r(t - \tau) \dot{z}(\tau) d\tau, \tag{6}$$

where m_∞ represents the mass and added mass at infinite frequency of the buoy. $k_r(t)$ is the impulse response function (IRF) of the radiation force, which can be obtained by:

$$k_r = \frac{2}{\pi} \int_0^\infty B_z(\omega) \cos(\omega t) d\omega, \tag{7}$$

Wave excitation and radiation forces are modeled using linear hydrodynamic coefficients, including added mass and radiation damping coefficients. ANSYS-AQWA 2020 is a standard simulation package, and it can calculate these hydrodynamic parameters using a frequency domain potential flow boundary element method (BEM) solver. The BEM solutions of added mass and radiation coefficients are obtained by solving the Laplace equation for the velocity potential of the float, which assumes that the flow is inviscid, incompressible, and irrotational [56]. The added mass A_z and radiation damping B_z are shown in Figure 4.

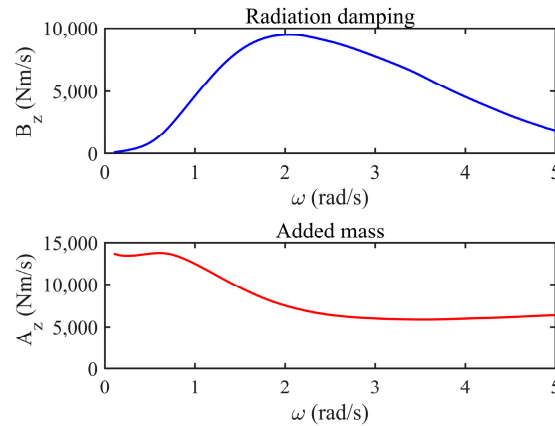


Figure 4. Added mass A_z and radiation damping B_z .

In order to improve the calculation speed of the radiation force, a state space model (SSM) was used instead of the convolution integral term $\int_0^t \tilde{k}_r(t - \tau) \dot{z}(\tau) d\tau$.

$$\begin{cases} \dot{\mathbf{X}}(t) = \mathbf{A}\mathbf{X}(t) + \mathbf{B}\dot{z}_1(t) \\ \int_0^t \tilde{k}_r(t - \tau) \dot{z}(\tau) d\tau = \mathbf{C}\mathbf{X}(t)' \end{cases} \tag{8}$$

where $\mathbf{X}(t)$ is the n -order state vector. \mathbf{A} , \mathbf{B} , and \mathbf{C} are constant coefficient matrices of the SSM. $\tilde{k}_r(t)$ is the approximate value of $k_r(t)$. $\dot{z}_1(\tau)$ is the velocity of the buoy. \mathbf{A} , \mathbf{B} , and \mathbf{C} are constant coefficient matrices of the state space model that can be determined using the realization theory approach.

$$\mathbf{A} = \begin{bmatrix} -5.539 & -51.02 & -176.5 & -646.6 & -991.7 & -978.8 \\ 1 & 0 & 0 & 0 & 0 & 0 \\ 0 & 1 & 0 & 0 & 0 & 0 \\ 0 & 0 & 1 & 0 & 0 & 0 \\ 0 & 0 & 0 & 1 & 0 & 0 \\ 0 & 0 & 0 & 0 & 1 & 0 \end{bmatrix}$$

$$\mathbf{B} = [1 \ 0 \ 0 \ 0 \ 0 \ 0]^T$$

$$\mathbf{C} = [17340 \ 98150 \ 745500 \ 2352000 \ 6298000 \ -82460]$$

In the time domain, the hydrostatic restoring force F_{hs} can be expressed as:

$$F_{hs} = -\frac{1}{4}\rho g\pi D_2^2 z_1(t), \tag{9}$$

where D_2 is the diameter of the float, and $D_2 = 4$ m in this study.

Figure 5 shows the equivalent magnetic charge model for coaxial inner and outer sector magnets. The axial magnetic force of the NSM F_m can be calculated based on the equivalent magnetic charge theory [28].

$$F_m = \frac{B_r^2}{\pi\mu_0} \int_0^\alpha \int_{\frac{\pi}{2}-\alpha}^{\frac{\pi}{2}} \int_{R_1}^{R_2} \int_{R_3}^{R_4} \left(\frac{z_{13}^{(r)}}{|\vec{r}_{13}^{(r)}|} + \frac{z_{24}^{(r)}}{|\vec{r}_{24}^{(r)}|} - \frac{z_{23}^{(r)}}{|\vec{r}_{23}^{(r)}|} - \frac{z_{14}^{(r)}}{|\vec{r}_{14}^{(r)}|} \right) r_1 r_2 dr_1 dr_2 d\theta d\delta - \tag{10}$$

$$\frac{B_r^2}{\pi\mu_0} \int_0^\alpha \int_{\frac{\pi}{2}}^{\frac{\pi}{2}+\alpha} \int_{R_1}^{R_2} \int_{R_3}^{R_4} \left(\frac{z_{13}^{(a)}}{|\vec{r}_{13}^{(a)}|} + \frac{z_{24}^{(a)}}{|\vec{r}_{24}^{(a)}|} - \frac{z_{23}^{(a)}}{|\vec{r}_{23}^{(a)}|} - \frac{z_{14}^{(a)}}{|\vec{r}_{14}^{(a)}|} \right) r_1 r_2 dr_1 dr_2 d\theta d\delta,$$

where P_i is a point on the magnetic pole surface S_i of the inner sector magnet ($i = 1,2$), and P_j is a point on the magnetic pole surface S_j of the outer sector magnet ($j = 3,4$). \vec{r}_{ij} is the position vector between points P_i and P_j , and z_{ij} is the axial component of \vec{r}_{ij} . The superscripts (r) and (a) denote repulsive and attractive magnets, respectively. B_r is the residual magnetic flux density. μ_0 is the vacuum permeability.

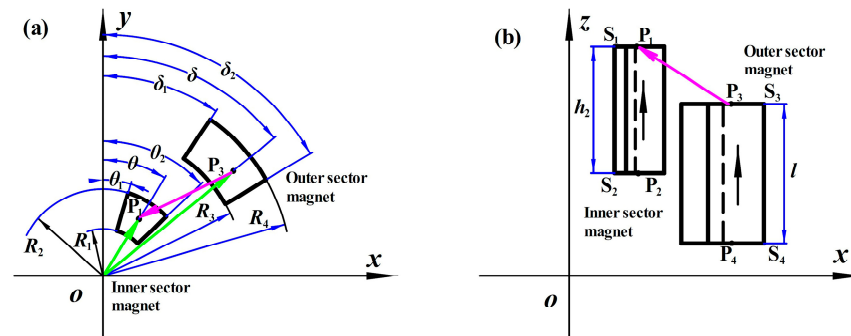


Figure 5. Equivalent magnetic charge model for coaxial inner and outer sector magnets. (a) Front view of the magnetic charge model, (b) Top view of the magnetic charge model.

The reaction force of the hydraulic PTO system acting on the buoy can be calculated by:

$$F_{PTO} = (p_t - p_b)A_p, \tag{11}$$

$$A_p = \pi(R_p^2 - R_r^2), \tag{12}$$

where R_p and R_r are the radius of piston and rod, respectively. p_t and p_b are the oil pressure of the upper and bottom chamber of hydraulic cylinder, respectively. The value of p_t is approximately equal to the accumulator pressure p_{ac} , which can be given by [49]:

$$p_t = p_{ac}, \tag{13}$$

$$\frac{\dot{p}_{ac}}{p_{pre}} = -\kappa \frac{q_{ac}}{V_{g0}}, \tag{14}$$

where p_{pre} is the pre-charged gas pressure of the accumulator; V_{g0} is the initial gas pressure of the accumulator; κ is the gas adiabatic index; and q_{ac} denotes the flow rate of oil into the accumulator. q_{ac} can be obtained by

$$q_{ac} = q_t - q_v, \tag{15}$$

$$q_t = (z_1 - z_2)A_p, \tag{16}$$

where q_t denotes the flow rate of oil out of the upper chamber and q_v denotes the outlet flow rate of the throttle valve.

The throttle valve is used to regulate the oil flow into the hydraulic motor. In this study, the outlet flow rate of the throttle valve can be expressed by [49]:

$$q_v = C_d A_v \sqrt{\frac{2(p_M - p_{ac})}{\rho_0}}, \tag{17}$$

where C_d is the flow coefficient, A_v denotes the valve port through-flow area, p_M is the oil pressure at the inlet of the hydraulic motor, and ρ_0 is the density of the hydraulic oil.

Neglecting the compressibility and leakage of the hydraulic oil, the angular velocity ω_M of the hydraulic motor can be determined by:

$$q_M = D_M \omega_M, \tag{18}$$

where q_M is the flow rate into the hydraulic motor, $q_M = q_v$, and D_M is the displacement of the hydraulic motor.

The kinetic equations for the hydraulic motor and generator are given by:

$$J_t \dot{\omega}_M = D_M(p_M - p_{tank}) - T_G, \tag{19}$$

where J_t is the total rotational inertia of the hydraulic motor and generator, p_{tank} is the tank pressure taken as 0, and T_G is the resistive torque of the permanent magnet synchronous generator. When the electrical load is purely resistive, the value of T_G can be calculated by

$$T_G = \frac{E^2}{R\omega_G}, \tag{20}$$

where R is the load resistance; ω_G is the angular velocity of the generator, $\omega_G = \omega_M$; and E is the phase electromotive force of the generator, which can be calculated by

$$E = \frac{4.44Nk_e u n_G \phi_e}{60}, \tag{21}$$

where N is the number of series turns per phase winding; k_e is the electromotive force winding factor; u is the number of pole pairs of the generator armature windings; ϕ_e is the magnetic flux; and n_G is the generator rotational speed with $n_G = 2\pi\omega_G$.

The mean output power of the generator during period t to $t + T$ can be defined as

$$P_i = \frac{E^2}{R}, \tag{22}$$

$$P_m = \frac{1}{T} \int_t^{t+T} P_{Gi} dt, \tag{23}$$

where P_i is the instantaneous power of the generator, and P_m is the mean power of the generator.

To evaluate the motion response of the nonlinear EIWEC, the buoy, mass, and relative RAOs are defined as [40]:

$$RAO_1 = \frac{\max(z_1)}{A}, \tag{24}$$

$$RAO_2 = \frac{\max(z_2)}{A}, \tag{25}$$

$$RAO_3 = \frac{\max(z_3)}{A}, \tag{26}$$

where A is the wave amplitude.

2.3. Software Application and Configuration

The calculation framework of this study is shown in Figure 6. Wave excitation and radiation forces are modeled using linear hydrodynamic coefficients, including added mass and radiation damping coefficients, which can be obtained by ANSYS-AQWA. A joint simulation calculation between MATLAB/Simulink 2020 and AMESim 2020 is applied for the time domain analysis. The former provides the motion response signals to the latter, and the latter transmits the computed PTO forces to the former.

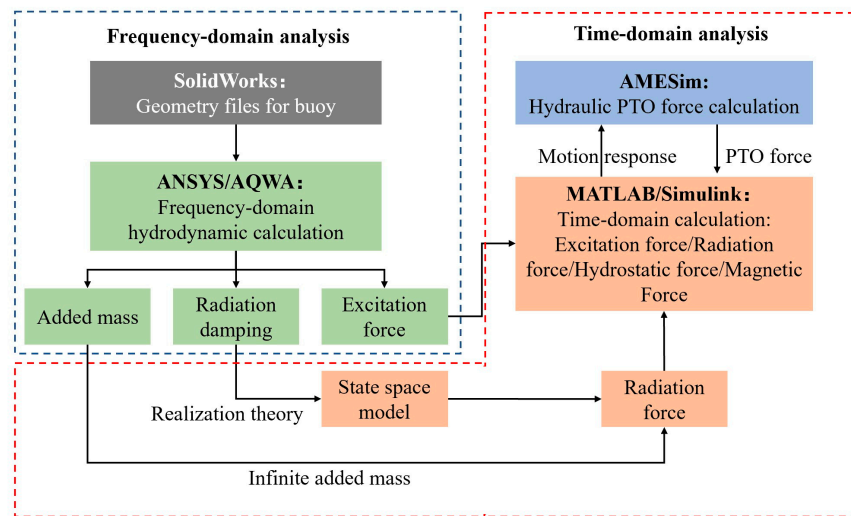


Figure 6. Calculation framework.

2.4. Validation of the Time-Domain Model

To validate the time-domain model of the WEC based on the state space model in this study, the results were compared with published works. The response amplitude operator (RAO) for the heave motion of the WEC system reported by Tampier and Grueter [57] was used for comparison. From Figure 7, the simulation results are in good agreement with the previously reported results, indicating that the proposed time-domain simulation model can accurately simulate the motion response.

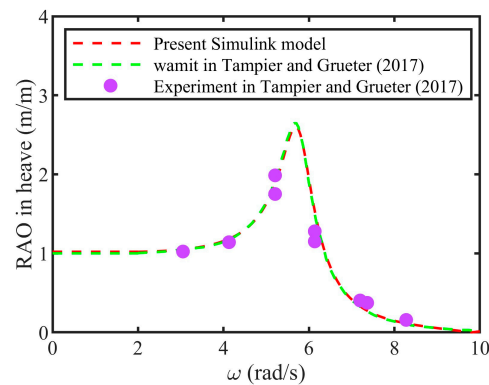


Figure 7. Comparison of RAO in heave obtained from the present time-domain model and simulation and experimental results reported by Tampier and Grueter (2017) [57].

3. Results and Discussion

3.1. Mechanical Property Analysis of NSM

3.1.1. Structural Parameters

The structural parameters of NSM are shown in Table 1. The outer magnetic ring comprises four attractive magnets and four repulsive magnets. The attractive and repulsive magnets have the same inner and outer diameters, and their height difference is Δh .

Table 1. Structural parameters of NSM.

Parameter	Symbol	Value
Inner diameter of inner magnetic rings (m)	R_1	0.2
External diameter of inner magnetic rings (m)	R_2	0.5
Inner diameter of outer magnetic rings (m)	R_3	0.6
External diameter of outer magnetic rings (m)	R_4	1.0
Center angle of attractive magnet ($^\circ$)	α	18
Center angle of repulsive magnet ($^\circ$)	$90^\circ - \alpha$	72
Height difference between attractive and repulsive magnets (m)	Δh	0.08
Height of inner magnetic ring (m)	h_1	0.15
Permeability of vacuum (H/m)	μ_0	$4\pi \times 10^{-7}$
Residual magnetic flux density (T)	B_r	1.25

3.1.2. Magnetic Force and Stiffness of NSM

Figure 8a shows the magnetic force F_m as a function of displacement z_1 , and the corresponding stiffness curves of the NSM are shown in Figure 8b. For comparison, the variation curves of hydrostatic force F_{hs} and hydrostatic stiffness k_{hs} are also plotted in Figure 8.

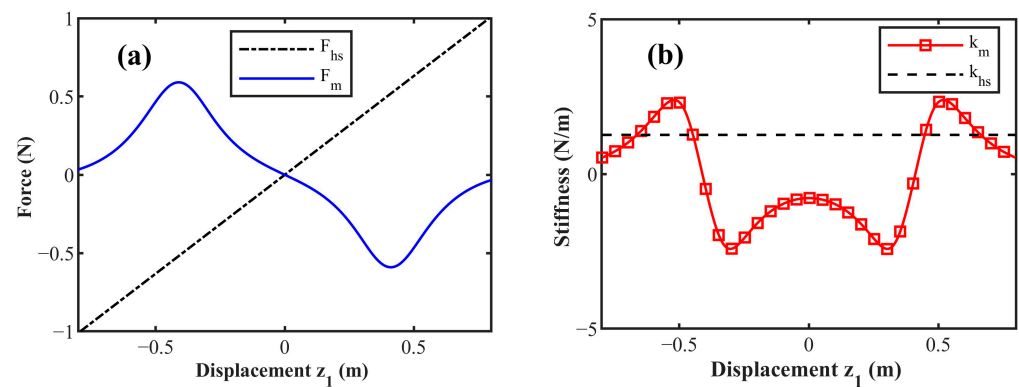


Figure 8. (a) Magnetic force of NSM, (b) stiffness of NSM.

From Figure 8a, because of the difference in magnetic field strength at various positions, the magnetic force and stiffness of the inner magnetic ring exhibit a nonlinear variation. At some positions, the NSM exhibits negative stiffness properties and has a good potential for improving the frequency bandwidth and energy conversion efficiency of energy harvesting systems. To investigate the effect of NSM on the EIWEC, we further analyzed the motion response and output power of the nonlinear EIWEC in Section 3.2.

3.2. Effect of Nonlinear Stiffness Mechanism (NSM)

3.2.1. Motion Response Analysis

Figure 9 illustrates the RAO as a function of frequency for linear and nonlinear EIWECs with different k . The simulation was executed for 300 s at each wave frequency (the calculation time step is 0.01 s.), and then the maximum motion response amplitude in the time range of 150 s to 300 s was then extracted as RAOs to eliminate transient effects in

the initial stage. As depicted in Figure 9, the RAOs of the linear and nonlinear EIWECs are plotted by blue dashed and red dotted lines, respectively. Notably, the maximum stroke limit (end-stops) of the buoy for the device is ± 4 m. All of the displacements in Figure 9 are within the range. When the wave frequency is less than 1 rad/s, the RAOs of the buoy and mass body of the linear EIWEC remain around 1, and the relative motion between the buoy and mass body is small. As the wave frequency increases, the motion response of the buoy and mass body first increases and then decreases. According to Figure 9c,f,i, the frequency bandwidth of the linear EIWEC is narrower compared with the nonlinear EIWEC. Accordingly, the linear EIWEC is not capable of adequately capturing energy from the wide frequency band of the ocean waves, leaving most of the wave energy unutilized.

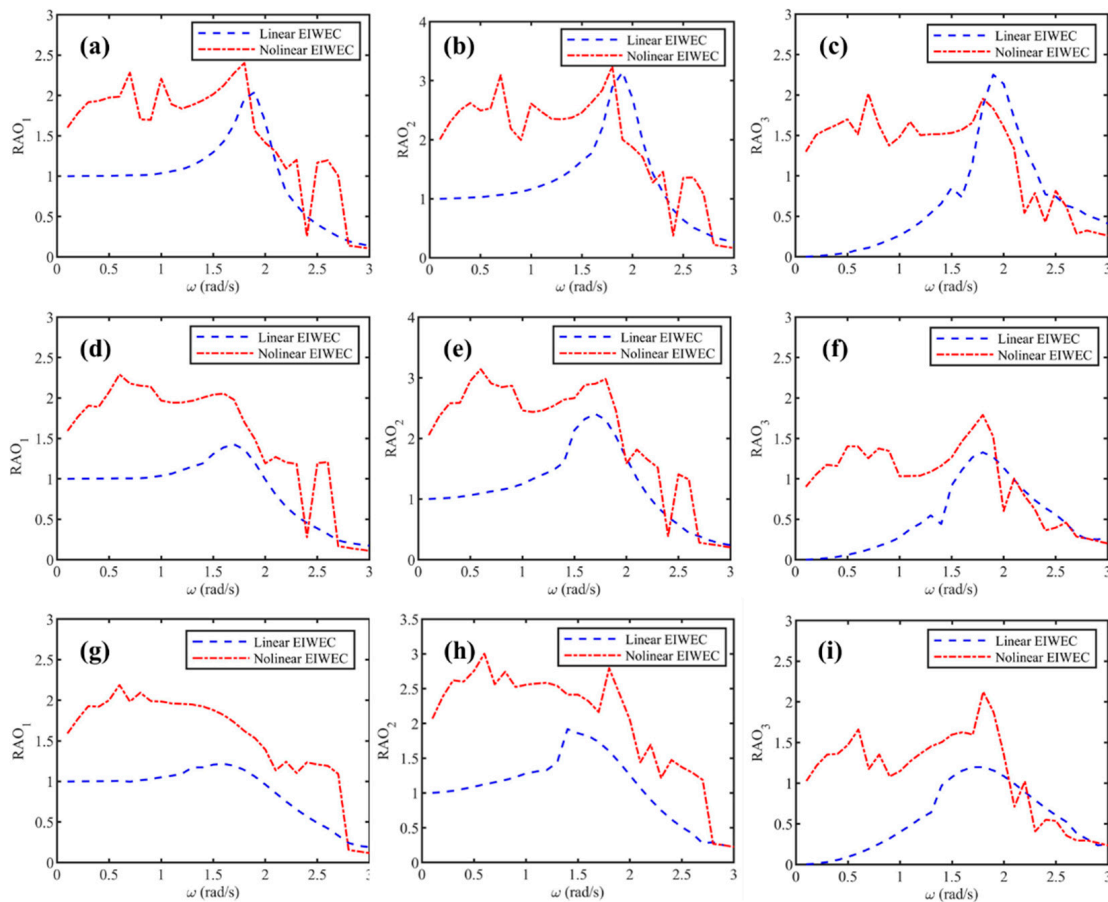


Figure 9. RAOs of the buoy, mass body, and relative motion. (a–c) $\Delta l = 1$ m; (d–f) $\Delta l = 2$ m; (g–i) $\Delta l = 3$ m. Simulation conditions: $m_2 = 6670$ kg, $D_m = 80$ cc/rev, $R = 50 \Omega$, $p_{pre} = 30$ bar, and $V_{g0} = 40$ L.

For a linear EIWEC, it resonates around 1.7 rad/s. Wave frequencies below or above this value will cause a significant power reduction. According to Figure 8, the NSM has a negative stiffness property, which can reduce the system’s natural frequency. Therefore, when the wave frequency is less than 1.7 rad/s, the nonlinear EIWEC is close to the resonant state, and the RAOs of relative motion are much higher than those of linear EIWEC. The large amplitude relative motion provides favorable conditions for energy transfer and conversion, contributing to the increase in output power of the EIWEC.

Meanwhile, the resonant frequency of the system is no longer a fixed value because of the influence of the nonlinear stiffness property, resulting in multiple resonance peaks in the RAOs curve of the nonlinear EIWEC. These characteristics effectively increase the frequency bandwidth of the EIWEC system, enabling EIWEC to be more robust in the face of the change in sea state. When the wave frequency is greater than 1.7 rad/s, the

negative stiffness property of NSM causes frequency detuning of the EIWEC, and the low natural frequency of the nonlinear EIWEC cannot match the high-frequency incident wave. Therefore, the motion response of the nonlinear EIWEC decreases rapidly with strong fluctuations. The response reduction for the nonlinear EIWEC occurs at periods of about 3.7 s. These results indicate that the nonlinear EIWEC is not adept at capturing wave energy from high-frequency components, and its performance may even be lower than linear EIWEC under some frequency conditions. However, this period value is relatively low in actual waves and may not be of practical interest. According to Falnes et al. [25], the wave period range is typically between 5 s and 15 s. In this period range, the motion response of the nonlinear EIWEC is consistently at high values, which shows good development potential for extracting energy from actual waves.

Meanwhile, the RAO curves of the nonlinear EIWEC show irregular fluctuations as the frequency changes. The fluctuations may produce erratic, chaotic behavior and wear out the device more in the long term. To explain the reason for the fluctuations and avoid those sudden downward spike regions, we further analyzed the motion response of the nonlinear EIWEC at different frequencies in terms of nonlinear dynamics.

Figure 10 illustrates the phase trajectories of the motion response of the buoy and the internal mass body for nonlinear EIWECs with different spring stiffnesses when the wave frequencies are 2.3 rad/s, 2.4 rad/s, and 2.5 rad/s, respectively.

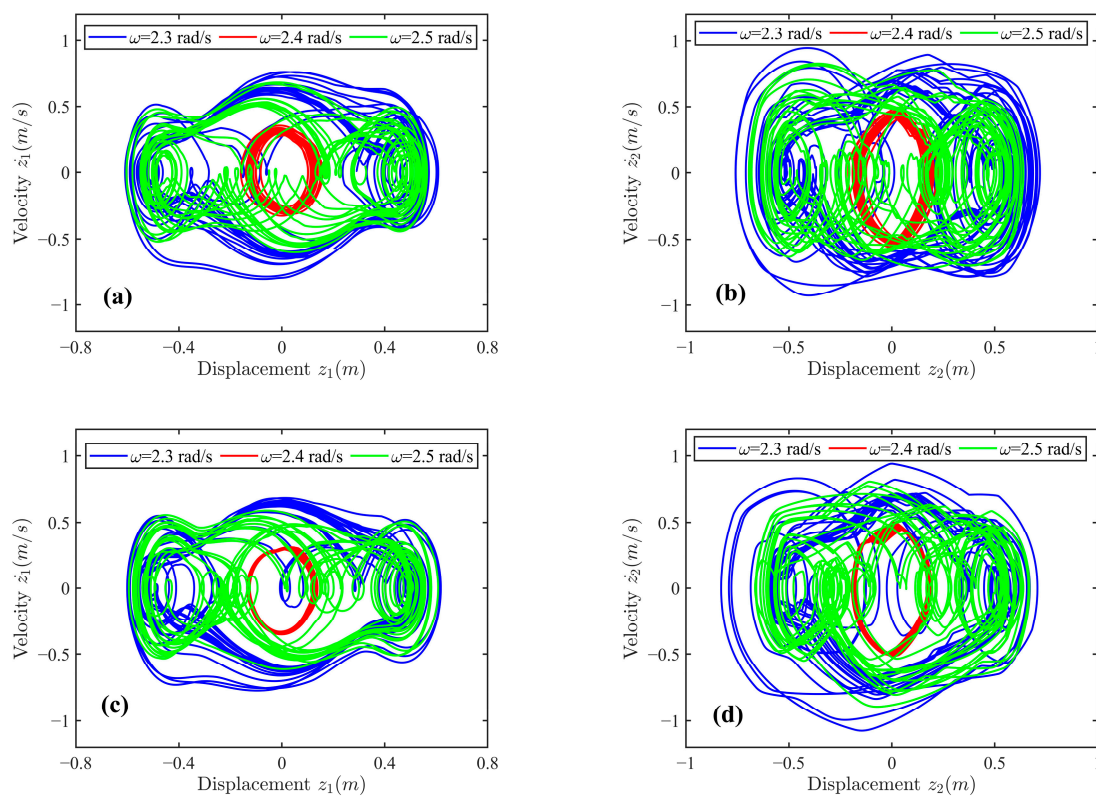


Figure 10. Phase trajectories of the motion response of the buoy and the internal mass body for nonlinear EIWECs with different spring stiffnesses when the wave frequencies are 2.3 rad/s, 2.4 rad/s, and 2.5 rad/s, respectively. (a,b) $\Delta l = 1$ m; (c,d) $\Delta l = 2$ m.

From Figure 10, when the wave frequencies are 2.3 rad/s and 2.5 rad/s, the buoy and internal mass body of the nonlinear EIWEC produce complex chaotic motions. The chaotic motion is irregular and contains inter-well and intra-well components, making the energy output strongly random and fluctuating. At a wave frequency of 2.4 rad/s, the buoy and the internal mass body are trapped in the middle potential well and can only produce intra-well motion, causing a sudden drop in the output power. In practice, a nonlinear

stiffness mechanism might make the system more sensitive at high-frequency conditions (greater than the resonance frequency), and the EIWEC produces complex and diverse nonlinear motions, resulting in irregularities in the RAOs curves.

The stiffness of the nonlinear mechanism changes drastically around -0.5 m and 0.5 m. In order to investigate the effect of the change on the system, the phase trajectories of the buoys of linear and nonlinear EIWEC are plotted for different stiffness conditions when the wave height is 1 m and the frequency is 1 rad/s, as illustrated in Figure 11.

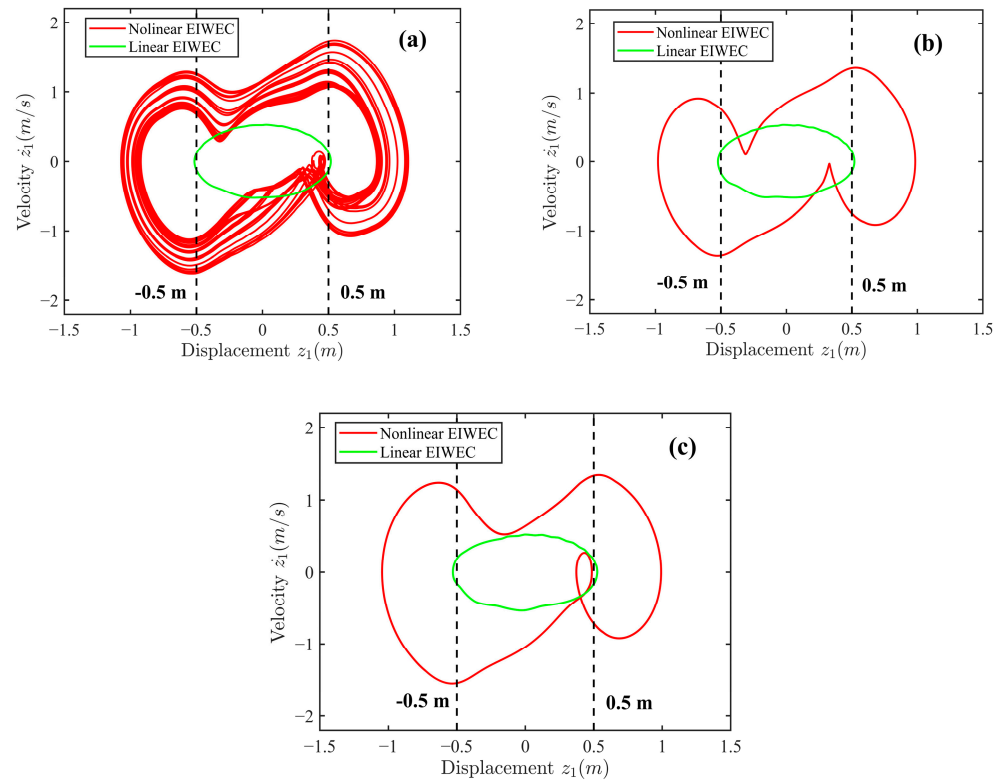


Figure 11. Phase trajectories of the buoys of linear and nonlinear EIWEC for different stiffness conditions when the wave height is 1 m and the frequency is 1 rad/s. (a) $\Delta l = 1$ m; (b) $\Delta l = 2$ m; (c) $\Delta l = 3$ m.

For the nonlinear EIWEC, the velocity of the buoy changes drastically at these two positions, which could cause fluctuations in the energy output. Interestingly, these stiffness variations seem to bring remarkable gains to the system. For the linear EIWEC, the motion response of the buoy is limited to these two threshold intervals. Due to the stiffness variations, the motion response of the float increases rapidly for the nonlinear EIWEC, which favors the power output capability of the system.

3.2.2. Output Power Analysis

Figure 12a,b show the variation of output power for linear and nonlinear EIWECs under different ω and Δl , respectively. The mapping distribution of output power in the $(\omega, \Delta l)$ space is illustrated in Figure 12c,d. When the wave frequency is less than 1 rad/s, the output power of the linear EIWEC is nearly 0 W because of the small relative displacement z_3 . The system exhibits a single resonance peak, and the output power initially increases and then decreases with the increase in wave frequency (Figure 12a). The effective frequency bandwidth of a linear EIWEC strongly correlates with the linear spring. The frequency bandwidth of the linear EIWEC gradually increases as initial elongation Δl increases (Figure 12c). Therefore, selecting a larger Δl facilitates the linear EIWEC to harvest energy from a wider range of wave frequencies and improves the system's energy

capture performance. However, it is unreasonable and difficult to select a linear spring with excessive Δl for the EIWEC due to the limited internal space of the buoy.

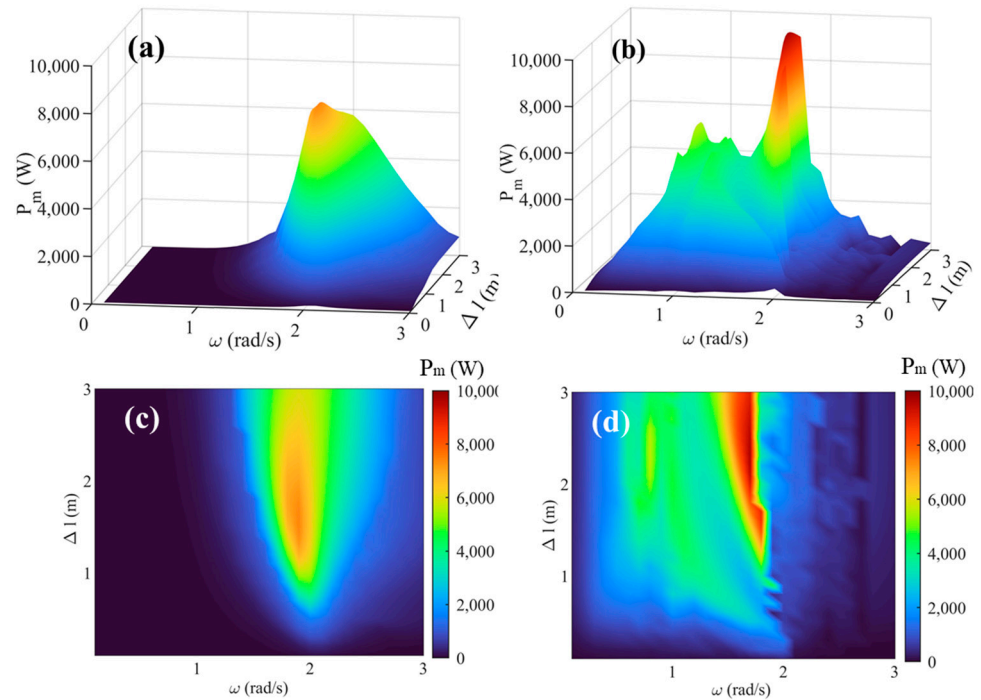


Figure 12. Distribution of generation power in the $(\omega, \Delta l)$ space. (a,c): Linear EIWEC; (b,d) nonlinear EIWEC. Simulation conditions: $m_2 = 6670$ kg, $D_m = 80$ cc/rev, $R = 50 \Omega$, $p_{pre} = 30$ bar, and $V_{g0} = 40$ L.

As shown in Figure 12b, the output power of nonlinear EIWEC is noticeably improved compared to linear EIWEC. The negative stiffness of NSM reduces the intrinsic frequency of the EIWEC system, which facilitates the system to resonate more easily under low frequency wave conditions. The effective frequency band of the system shifts to a lower frequency range, and the output power and frequency bandwidth of the EIWEC is considerably enhanced. Additionally, the NSM decreases the correlation between the linear spring stiffness and the frequency bandwidth. In the frequency range from 0.4 to 1.5 rad/s, the output power of the system is insensitive to changes in the wave frequencies and linear spring stiffness. These characteristics increase the power output robustness of the EIWEC against sea state changes and reduce the design difficulty of the linear spring.

3.3. Effect of Mass Body and Linear Spring

The mass body and linear spring of EIWEC are the critical components for energy harvesting and conversion. This section investigates the effect of mass ratio γ of the internal mass body and initial elongation Δl of the linear spring on the performance of the nonlinear EIWEC. The mass ratio γ is defined by Equation (27). Ocean waves typically have periods between 5 and 15 s (0.42 rad/s to 1.26 rad/s). Figure 13 shows the output power of nonlinear EIWEC as a function of γ and Δl under typical wave period conditions ($T = 5$ s, 7.5 s, 10 s, 12.5 s, and 15 s).

$$\gamma = m_2 / (m_1 + m_2) \tag{27}$$

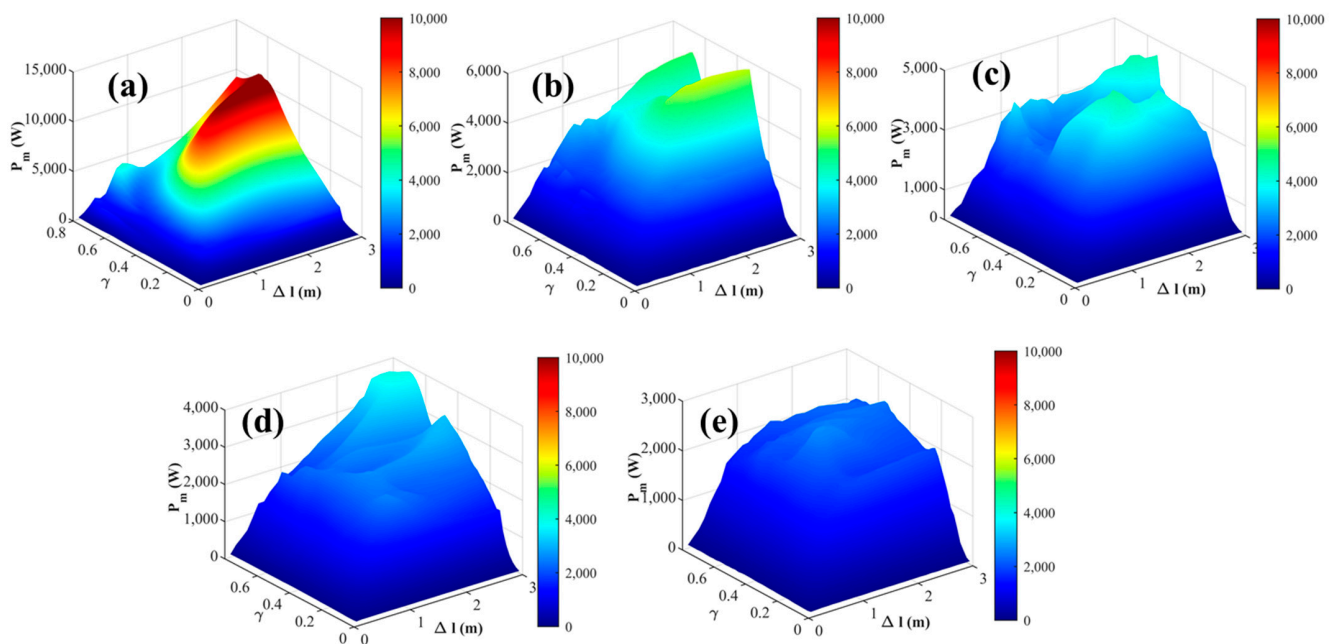


Figure 13. Output power of nonlinear EIWECs as a function of γ and Δl under typical wave period conditions. (a) $T = 5$ s, (b) $T = 7.5$ s, (c) $T = 10$ s, (d) $T = 12.5$ s, and (e) $T = 15$ s.

There are some differences in the power distribution of the system under various wave periods. As illustrated in Figure 13a, when the wave period is 5 s, nonlinear EIWEC can obtain higher output power by selecting a larger mass ratio γ and initial elongation Δl . Within a reasonable parameter range, increasing the mass of the internal mass body and decreasing the stiffness of the linear spring will have a positive effect on enhancing the energy conversion performance of the system. According to Figures 9 and 12, the system is close to resonance at this time, and the influence of the NSM on the motion response and output power is reduced. The motion response of the system is close to optimal, and increasing the mass of the internal mass body can convert more wave energy into available kinetic energy. Therefore, in short-period wave scenarios, the nonlinear EIWEC is more sensitive to parameter variations in the internal mass body and linear spring. There are differences in wave conditions in different deployment areas. It is necessary to first determine the dominant wave frequency of the target deployment area. After that, the structural parameters (γ and Δl) will be determined according to this frequency to ensure maximum power output.

As the wave period increases to 7.5 s, 10 s, and 12.5 s, multiple high-power regions (red areas) appear in Figure 13b,c, and these high-power regions extend into the parameter domain of the low mass ratio and initial elongation. These results suggest that efficient energy conversion can also be achieved by choosing low mass ratios and large spring stiffnesses in seas dominated by medium wave periods, significantly reducing the design difficulty of mass bodies and linear springs. When the wave period is 15 s, the system's average power is insensitive to changes in the mass body and the linear spring. Nonlinear EIWECs with different mass ratios and initial elongations have similar energy conversion capabilities. At this time, the NSM plays a critical role in adjusting the intrinsic frequency of the system. When different internal mass bodies and linear springs are selected, the nonlinear negative stiffness characteristics of the NSM can adaptively modify the motion response to ensure the stable output of the system. Accordingly, the choice of parameters will become more convenient under long-period wave conditions.

3.4. Influence of Hydraulic PTO Parameters

3.4.1. Effect of Pre-Charged Pressure of Accumulator

The pre-charged pressure p_{pre} and initial gas volume V_{g0} are two critical parameters of an accumulator. Choosing different p_{pre} and V_{g0} affects the buffer capacity of the hydraulic PTO system, which will further change the efficiency and stability of the energy conversion and output. Sections 3.4.1 and 3.4.2 investigated the effect of the precharged pressure and initial gas volume of the accumulator on the average output power P_m and power standard deviation σ , respectively. Among them, the power standard deviation is used to measure the stability of the output power.

Figure 14a,b present the average output power P_m and power standard deviation σ as a function of the pre-charged pressure of accumulator p_{pre} , respectively. The output power of the system remains constant and the power standard deviation is relatively low when the pre-charged pressure p_{pre} is below 30 bar. Notably, a low σ means less pressure and flow fluctuations in the hydraulic PTO system and more stable output power produced by the generator.

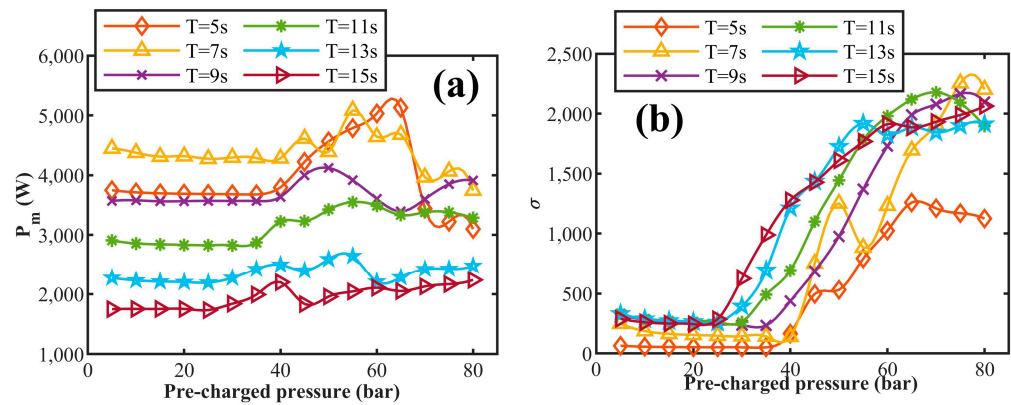


Figure 14. Average output power P_m and power standard deviation σ as a function of the pre-charged pressure of accumulator p_{pre} . (a) Average output power, (b) power standard deviation.

When p_{pre} was greater than 30 bar, the average output power changed significantly under all wave period conditions, and P_m showed an overall trend of increasing and then decreasing. As p_{pre} increases, the power standard deviation increases dramatically, and the electrical output stability of the PTO system deteriorates. These results suggest that choosing a lower pre-charged pressure of the accumulator can allow the pulsations in the hydraulic PTO system to be fully absorbed, which facilitates the improvement of the electric energy quality in nonlinear EIWEC. Although increasing the pre-charged pressure can improve the power generation of the system to some extent, it weakens the stability of the power output.

To further investigate the influence mechanism of the pre-charged pressure on the stability characteristics of the output power, Figure 15 illustrates the time-varying curves of accumulator inlet pressure q_{ac} , instantaneous power P_{Gi} , and PTO force F_{PTO} when $p_{pre} = 20$ bar and 60 bar, respectively. Due to the introduction of the NSM, the change in relative displacement z_3 increases, resulting in sharp pressure and flow pulsations in the hydraulic PTO system. When p_{pre} is set to 20 bar, the q_{ac} is steadily maintained at 40 bar (Figure 15a). The oil in the hydraulic line can flow continuously and smoothly into the hydraulic motor, ensuring the stability of generation power (Figure 15b). Meanwhile, the constant pressure allows the hydraulic system to provide smooth PTO force (Figure 15c), helping to improve the work reliability and service life of the hydraulic cylinder. When $p_{pre} = 60$ bar, the accumulator can only open and release the oil to flow into the hydraulic motor when the system pressure accumulates to 60 bar. As illustrated in Figure 15a,b, the excessive p_{pre} causes discontinuity in the oil flow and intermittent operating issues in the PTO system. Consequently, the power output of the generator exhibits unstable

fluctuations resembling a sawtooth pattern. Additionally, the intermittent pulsations of pressure and flow can cause high-frequency vibration in the hydraulic components, potentially compromising the reliability of the sealing elements and valve body.

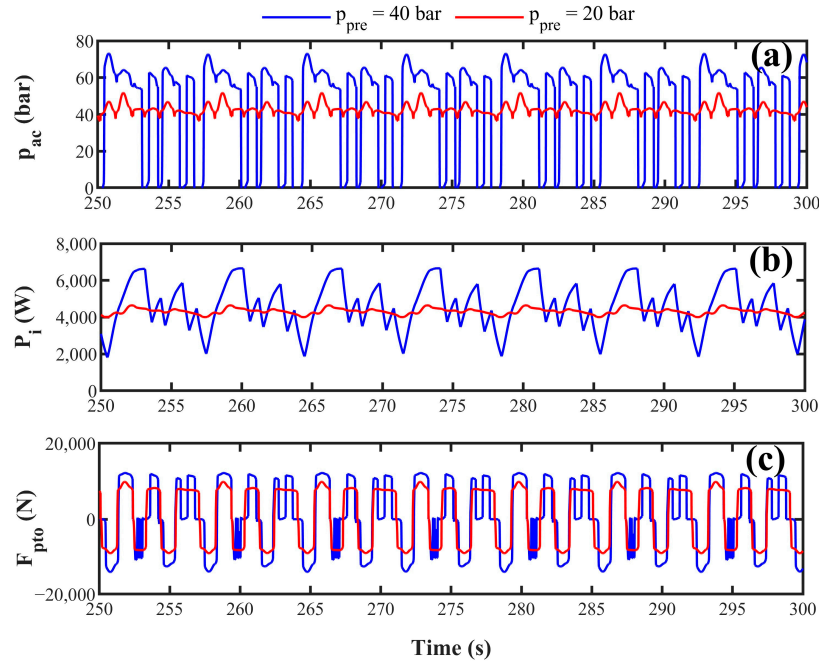


Figure 15. Time-varying curves corresponding to the pre-charged pressures of 20 bar and 60 bar when the wave height is 1 m and the period is 7 s. (a) accumulator inlet pressure q_{ac} , (b) instantaneous power P_i , and (c) PTO force F_{PTO} .

3.4.2. Effect of the Initial Gas Volume of the Accumulator

The initial gas volume of the accumulator V_{g0} plays the role of a buffer spring. Different initial gas volumes can affect the absorption effect of flow and pressure pulsations in the hydraulic system and change the dynamics and power output characteristics of nonlinear EIWEC. Figure 16a,b show the variation in the average output power and power standard deviation with the initial gas volume of accumulator V_{g0} , respectively.

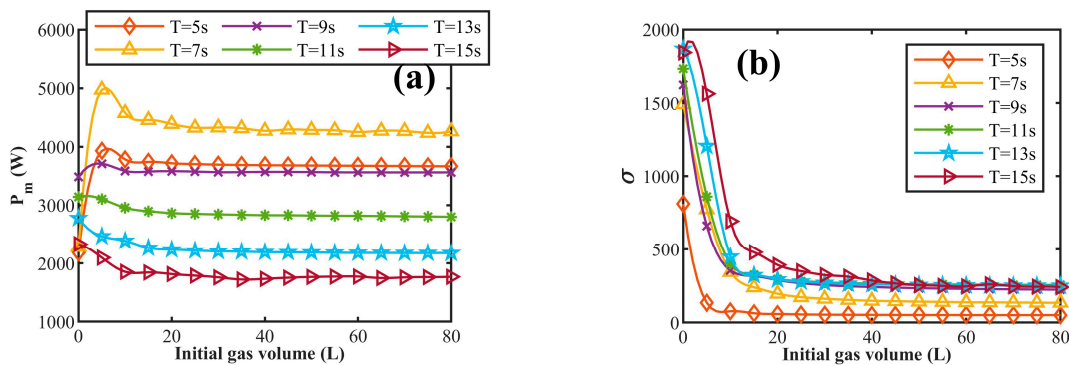


Figure 16. Variation in the average output power and power standard deviation with the initial gas volume of accumulator V_{g0} . (a) Average output power, (b) power standard deviation.

As shown in Figure 16a, under short period wave conditions ($T = 5 \text{ s}$, 7 s , and 9 s), as V_{g0} increases, the output power of the system first increases and then decreases and finally tends to a constant. For medium and long period waves ($T = 11 \text{ s}$, 13 s , and 15 s), the effect of initial gas volume on output power is relatively small. The increase in V_{g0} causes the average output power to decrease slightly and quickly tends towards a constant

value. According to Figure 16b, when V_{g0} is less than 10 L, the power standard deviation is relatively high, which indicates that the output power generated by the PTO system has a high degree of volatility. This is mainly because the accumulators with the small V_{g0} are of limited buffer capacity and incapable of adequately absorbing pressure and flow fluctuations in a hydraulic PTO system. The pressure and flow fluctuations will cause the hydraulic motor and generator speeds to vary dramatically, thus generating an unstable power output.

With the increase in V_{g0} , the buffer capacity of the accumulator is enhanced, and the power standard deviation decreases rapidly to a constant value. This indicates that increasing the initial gas volume of the accumulator V_{g0} helps reduce electricity fluctuations and improve output power stability in the hydraulic PTO system. Accordingly, under the premise of meeting the installation space requirements, selecting an accumulator with a larger initial gas volume can enhance the quality of electrical output. For the proposed nonlinear EIWEC system, an accumulator gas volume of at least 10 L is required to ensure optimal energy conversion performance.

3.4.3. Effect of Diameter of Throttle Valve

The throttle valve is installed at the inlet of the hydraulic motor to control the flow of the hydraulic system. Figure 17 shows the average output power of the nonlinear EIWEC as a function of diameter of throttle valve D_v .

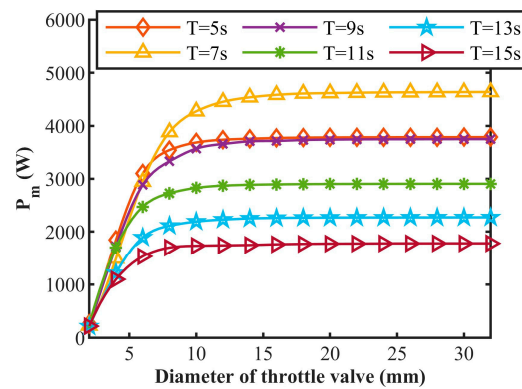


Figure 17. Average output power of the nonlinear EIWEC as a function of throttle diameter D_v . Simulation conditions: $m_2 = 6670$ kg, $D_m = 80$ cc/rev, $R = 50 \Omega$, $p_{pre} = 25$ bar, and $V_{g0} = 40$ L.

As D_v increases, the output power gradually increases and then remains constant. When the throttle diameter is less than 10 mm, the control effect of the throttle is more pronounced, and the output power of the system is proportional to the diameter of the throttle valve. Within this parameter range, changing the value of D_v can regulate the flow rate of the hydraulic system and the speed of the hydraulic motor to control the electrical performance of the nonlinear EIWEC system. As D_v continues to increase, the through-flow area of the throttle valve increases. The local pressure drops caused by the throttle valve gradually decrease, and the flow rate and output power of the hydraulic system tend to stabilize.

3.4.4. Effect of Displacement of the Hydraulic Motor and Load Resistance

The displacement of the hydraulic motor and the load resistance directly affect the torque of the generator, which in turn changes the power output and dynamic response of the PTO system. Therefore, this subsection further investigates the effect of the displacement of hydraulic motor D_m and the load resistance R on system performance.

Figure 18 shows the variation in the output power of nonlinear EIWEC with wave frequency under different D_m and R conditions. When $R = 10 \Omega$, increasing D_m helps to improve the energy conversion performance of the nonlinear EIWEC. As D_m increases, the output power of the system gradually rises. Meanwhile, the nonlinear EIWEC system

transitions from a single-peak frequency response to a multi-peak frequency response, effectively expanding the frequency bandwidth and work efficiency of the system. Consequently, the nonlinear EIWEC can exhibit stronger robustness in the face of the change in wave frequencies.

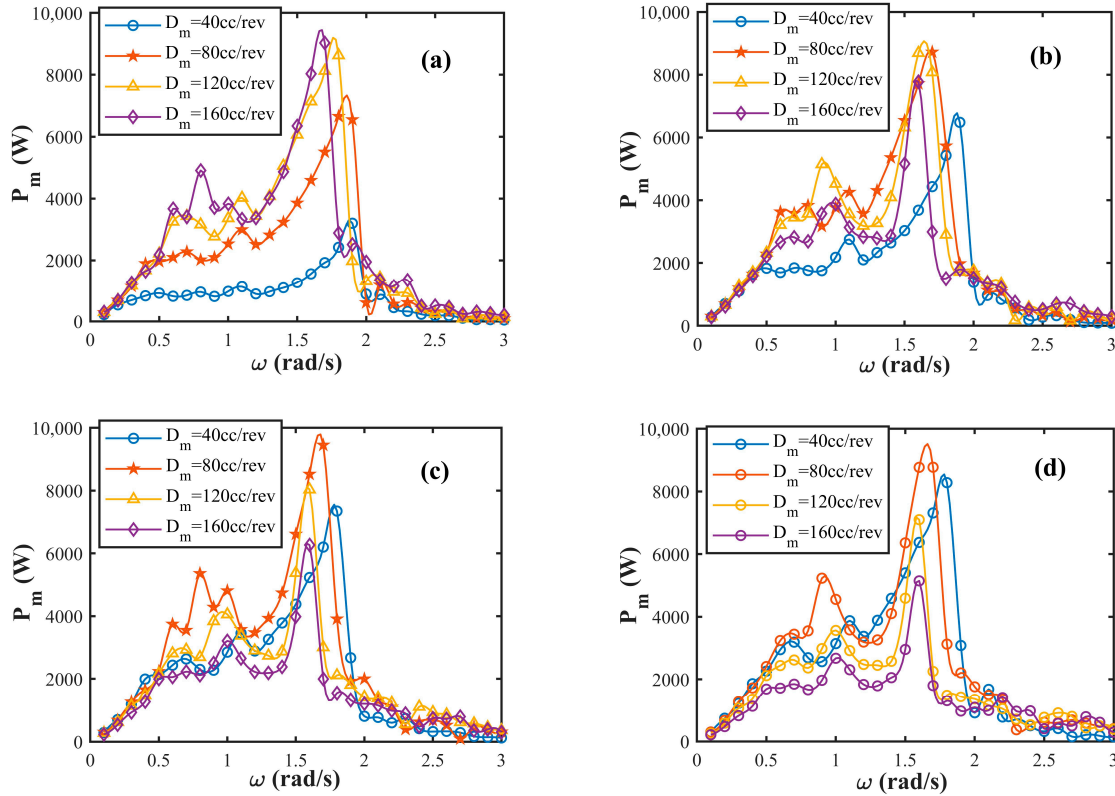


Figure 18. Variation in the output power of nonlinear EIWEC with wave frequency under different displacements of the hydraulic motor and load resistance conditions. (a) 10 Ω, (b) 30 Ω, (c) 50 Ω, and (d) 70 Ω. Simulation conditions: $m_2 = 6670$ kg, $p_{pre} = 25$ bar, and $V_{g0} = 40$ L.

As the load resistance increases, the output performance corresponding to small motor displacements (40 cc/rev and 80 cc/rev) gradually improves. Conversely, the energy conversion capability of large motor displacements (120 cc/rev and 160 cc/rev) gradually declines. These findings indicate the existence of optimal matching values between the displacement of the hydraulic motor and load resistance for the nonlinear EIWEC. Increasing the hydraulic motor displacement enhances the energy conversion performance when the equivalent resistance of the external load is low. Conversely, lowering D_m will be advantageous when the equivalent resistance of the external load is large.

4. Conclusions

This study proposed a nonlinear EIWEC. A mathematical model of the nonlinear EIWEC was established based on the Cummins equation and the equivalent magnetic charge method, and the joint simulations were carried out using MATLAB/Simulink 2020 and AMESim 2020 software. Performance evaluation and motion response analysis were conducted for linear and nonlinear EIWECs. The influence of different structural and hydraulic PTO parameters on the power performance of the system was analyzed to determine reasonable design parameters. The key conclusions are presented as follows:

- (1) Compared to linear EIWEC, the introduction of NSM increased the motion response of nonlinear EIWEC. The large amplitude relative motion provided favorable conditions for energy conversion.

- (2) The nonlinear negative stiffness property of the NSM reduced the intrinsic frequency and broadened the frequency bandwidth of the EIWEC. The effective frequency band shifted to a lower frequency range, and the output power of the nonlinear EIWEC was considerably enhanced.
- (3) Within the typical wave frequency range, the output power of the nonlinear EIWEC is insensitive to changes in the wave frequencies and linear spring stiffness. This not only increases the robustness of the system but also reduces the design difficulty of the linear spring.
- (4) Increasing the mass of the internal mass body and decreasing the stiffness of the linear spring will have a positive effect on enhancing the power performance of the system.
- (5) Choosing an accumulator with lower pre-charged pressure and larger gas initial volume can fully absorb the pressure and flow pulsations in the hydraulic PTO system, which is favorable to the smooth power output.

This study demonstrates the advantages of nonlinear stiffness mechanisms for application in enclosed inertial wave energy converters, and it focuses on parametric and performance analysis of the nonlinear EIWEC system. In the future, we will conduct wave-tank tests to confirm the reliability of the simulation results.

Author Contributions: Conceptualization, Methodology, Writing, and Editing, J.Q.; Investigation and Validation, Z.Z.; Investigation and Validation, X.S.; Reviewing, S.H.; Reviewing and Supervision, Y.L.; Reviewing and Editing, G.X. All authors have read and agreed to the published version of the manuscript.

Funding: This research was supported by the National Natural Science Foundation of China (52171265, U22A20242, 52001186) and the Natural Science Foundation of Shandong Province (ZR2020QE292, ZR2021ZD23).

Institutional Review Board Statement: Not applicable.

Informed Consent Statement: Not applicable.

Data Availability Statement: Data are contained within the article.

Conflicts of Interest: The authors declare no conflicts of interest.

References

1. Coyle, E.D.; Simmons, R.A. *Understanding the Global Energy Crisis*; Purdue University Press: West Lafayette, IN, USA, 2014; ISBN 1557536619.
2. Bodansky, D. The United Nations framework convention on climate change: A commentary. *Yale J. Int'l L.* **1993**, *18*, 451.
3. Schleussner, C.; Rogelj, J.; Schaeffer, M.; Lissner, T.; Licker, R.; Fischer, E.M.; Knutti, R.; Levermann, A.; Frieler, K.; Hare, W. Science and policy characteristics of the Paris Agreement temperature goal. *Nat. Clim. Chang.* **2016**, *6*, 827–835. [[CrossRef](#)]
4. Davis, M.; Moronkeji, A.; Ahiduzzaman, M.; Kumar, A. Assessment of renewable energy transition pathways for a fossil fuel-dependent electricity-producing jurisdiction. *Energy Sustain. Dev.* **2020**, *59*, 243–261. [[CrossRef](#)]
5. Vidal-Amaro, J.J.; Østergaard, P.A.; Sheinbaum-Pardo, C. Optimal energy mix for transitioning from fossil fuels to renewable energy sources—The case of the Mexican electricity system. *Appl. Energy* **2015**, *150*, 80–96. [[CrossRef](#)]
6. Halkos, G.E.; Gkampoura, E. Reviewing usage, potentials, and limitations of renewable energy sources. *Energies* **2020**, *13*, 2906. [[CrossRef](#)]
7. Guo, B.; Wang, T.; Jin, S.; Duan, S.; Yang, K.; Zhao, Y. A review of point absorber wave energy converters. *J. Mar. Sci. Eng.* **2022**, *10*, 1534. [[CrossRef](#)]
8. Yue, W.; Wang, Z.; Ding, W.; Sheng, S.; Zhang, Y.; Huang, Z.; Wang, W. Feasibility of Co-locating wave energy converters with offshore aquaculture: The Pioneering case study of China's Penghu platform. *Ocean Eng.* **2023**, *288*, 116039. [[CrossRef](#)]
9. Clemente, D.; Rosa-Santos, P.; Ferradosa, T.; Taveira-Pinto, F. Wave energy conversion energizing offshore aquaculture: Prospects along the Portuguese coastline. *Renew. Energy* **2023**, *204*, 347–358. [[CrossRef](#)]
10. Clemente, D.; Rosa-Santos, P.; Taveira-Pinto, F. On the potential synergies and applications of wave energy converters: A review. *Renew. Sustain. Energy Rev.* **2021**, *135*, 110162. [[CrossRef](#)]
11. Gallutia, D.; Fard, M.T.; Soto, M.G.; He, J. Recent advances in wave energy conversion systems: From wave theory to devices and control strategies. *Ocean Eng.* **2022**, *252*, 111105. [[CrossRef](#)]
12. Tiron, R.; Mallon, F.; Dias, F.; Reynaud, E.G. The challenging life of wave energy devices at sea: A few points to consider. *Renew. Sustain. Energy Rev.* **2015**, *43*, 1263–1272. [[CrossRef](#)]

13. Xue, G.; Qin, J.; Zhang, Z.; Huang, S.; Liu, Y. Experimental Investigation of Mooring Performance and Energy-Harvesting Performance of Eccentric Rotor Wave Energy Converter. *J. Mar. Sci. Eng.* **2022**, *10*, 1774. [CrossRef]
14. Cordonnier, J.; Gorintin, F.; De Cagny, A.; Clément, A.H.; Babarit, A. SEAREV: Case study of the development of a wave energy converter. *Renew. Energy* **2015**, *80*, 40–52. [CrossRef]
15. Pozzi, N.; Bracco, G.; Passione, B.; Sirigu, S.A.; Mattiazzo, G. PeWEC: Experimental validation of wave to PTO numerical model. *Ocean Eng.* **2018**, *167*, 114–129. [CrossRef]
16. Khedkar, K.; Nangia, N.; Thirumalaisamy, R.; Bhalla, A.P.S. The inertial sea wave energy converter (ISWEC) technology: Device-physics, multiphase modeling and simulations. *Ocean Eng.* **2021**, *229*, 108879. [CrossRef]
17. The Penguin Wave Energy Converter. Available online: <https://wello.eu/the-penguin-2/> (accessed on 9 January 2024).
18. Clemente, D.; Rosa-Santos, P.; Taveira-Pinto, F.; Martins, P. Influence of platform design and power take-off characteristics on the performance of the E-Motions wave energy converter. *Energy Conv. Manag.* **2021**, *244*, 114481. [CrossRef]
19. Scarcity of Resources, Climate Change. Available online: <https://seaturns.com/> (accessed on 9 January 2024).
20. Crowley, S.; Porter, R.; Taunton, D.J.; Wilson, P.A. Modelling of the WITT wave energy converter. *Renew. Energy* **2018**, *115*, 159–174. [CrossRef]
21. Maheen, M.H.; Yang, Y. Wave energy converters with rigid hull encapsulation: A review. *Sustain. Energy Technol. Assess.* **2023**, *57*, 103273.
22. Clemente, D.; Rosa-Santos, P.; Taveira-Pinto, F.; Martins, P. Experimental performance assessment of geometric hull designs for the E-Motions wave energy converter. *Ocean Eng.* **2022**, *260*, 111962. [CrossRef]
23. Ding, W.; Wang, K.; Mao, Z.; Cao, H. Layout optimization of an inertial energy harvester for miniature underwater mooring platforms. *Mar. Struct.* **2020**, *69*, 102681. [CrossRef]
24. Chen, Z.; Zhang, L.; Yeung, R.W. Analysis and optimization of a Dual Mass-Spring-Damper (DMSD) wave-energy converter with variable resonance capability. *Renew. Energy* **2019**, *131*, 1060–1072. [CrossRef]
25. Falnes, J.; Kurniawan, A. *Ocean Waves and Oscillating Systems: Linear Interactions Including Wave-Energy Extraction*; Cambridge University Press: Cambridge, UK, 2020; ISBN 1108481663.
26. Khasawneh, M.A.; Daqaq, M.F. Response behavior of bi-stable point wave energy absorbers under harmonic wave excitations. *Nonlinear Dyn.* **2022**, *109*, 371–391. [CrossRef]
27. Khasawneh, M.A.; Daqaq, M.F. Experimental assessment of the performance of a bi-stable point wave energy absorber under harmonic incident waves. *Ocean Eng.* **2023**, *280*, 114494. [CrossRef]
28. Qin, J.; Zhang, Z.; Zhang, Y.; Huang, S.; Liu, Y.; Xue, G. Design and performance evaluation of novel magnetic tristable wave energy converter. *Ocean Eng.* **2023**, *285*, 115424. [CrossRef]
29. Kurniawan, A.; Greaves, D.; Chaplin, J. Wave energy devices with compressible volumes. *Proc. R. Soc. A Math. Phys. Eng. Sci.* **2014**, *470*, 20140559. [CrossRef] [PubMed]
30. Pecher, A.; Kofoed, J.P. *Handbook of Ocean Wave Energy*; Springer Nature: Berlin, Germany, 2017.
31. Bracco, G.; Canale, M.; Cerone, V. Optimizing energy production of an inertial sea wave energy converter via model predictive control. *Control Eng. Pract.* **2020**, *96*, 104299. [CrossRef]
32. Vissio, G.; Valério, D.; Bracco, G.; Beirão, P.; Pozzi, N.; Mattiazzo, G. ISWEC linear quadratic regulator oscillating control. *Renew. Energy* **2017**, *103*, 372–382. [CrossRef]
33. Salcedo, F.; Ruiz-Minguela, P.; Rodriguez, R.; Ricci, P.; Santos, M. Oceantec: Sea trials of a quarter scale prototype. In Proceedings of the 8th European Wave and Tidal Energy Conference, Uppsala, Sweden, 7–10 September 2009; pp. 460–465.
34. Sirigu, S.A.; Bracco, G.; Bonfanti, M.; Dafnakis, P.; Mattiazzo, G. On-board sea state estimation method validation based on measured floater motion. *IFAC-PapersOnLine* **2018**, *51*, 68–73. [CrossRef]
35. Scapolan, M.; Tehrani, M.G.; Bonisoli, E. Energy harvesting using parametric resonant system due to time-varying damping. *Mech. Syst. Signal Proc.* **2016**, *79*, 149–165. [CrossRef]
36. Giorgi, G.; Faedo, N. Performance enhancement of a vibration energy harvester via harmonic time-varying damping: A pseudospectral-based approach. *Mech. Syst. Signal Proc.* **2022**, *165*, 108331. [CrossRef]
37. Yurchenko, D.; Alevras, P. Dynamics of the N-pendulum and its application to a wave energy converter concept. *Int. J. Dyn. Control* **2013**, *1*, 290–299. [CrossRef]
38. Giorgi, G. Embedding parametric resonance in a 2:1 wave energy converter to get a broader bandwidth. *Renew. Energy* **2023**, *222*, 119928. [CrossRef]
39. Schubert, B.W.; Sergiienko, N.Y.; Cazzolato, B.S.; Robertson, W.S.; Ghayesh, M.H. The true potential of nonlinear stiffness for point absorbing wave energy converters. *Ocean Eng.* **2022**, *245*, 110342. [CrossRef]
40. Guo, B.; Ringwood, J.V. Non-linear modeling of a vibro-impact wave energy converter. *IEEE Trans. Sustain. Energy* **2020**, *12*, 492–500. [CrossRef]
41. Zhang, H.; Xi, R.; Xu, D.; Wang, K.; Shi, Q.; Zhao, H.; Wu, B. Efficiency enhancement of a point wave energy converter with a magnetic bistable mechanism. *Energy* **2019**, *181*, 1152–1165. [CrossRef]
42. Zhang, X.; Tian, X.; Xiao, L.; Li, X.; Chen, L. Application of an adaptive bistable power capture mechanism to a point absorber wave energy converter. *Appl. Energy* **2018**, *228*, 450–467. [CrossRef]
43. Liu, B.; Yi, H.; Levi, C.; Estefen, S.F.; Wu, Z.; Duan, M. Improved bistable mechanism for wave energy harvesting. *Ocean Eng.* **2021**, *232*, 109139. [CrossRef]

44. Wang, L.; Tang, H.; Wu, Y. On a submerged wave energy converter with snap-through power take-off. *Appl. Ocean Res.* **2018**, *80*, 24–36. [[CrossRef](#)]
45. Todalshaug, J.H.; ásgeirsson, G.S.; Hjálmarsson, E.; Maillet, J.; Möller, P.; Pires, P.; Guérinel, M.; Lopes, M. Tank testing of an inherently phase-controlled wave energy converter. *Int. J. Mar. Energy* **2016**, *15*, 68–84. [[CrossRef](#)]
46. Corpower. Available online: <https://www.corpowerocean.com/> (accessed on 9 January 2024).
47. Li, M.; Jing, X. A bistable X-structured electromagnetic wave energy converter with a novel mechanical-motion-rectifier: Design, analysis, and experimental tests. *Energy Conv. Manag.* **2021**, *244*, 114466. [[CrossRef](#)]
48. Wang, Y.; Huang, S.; Xue, G.; Liu, Y. Influence of Hydraulic PTO Parameters on Power Capture and Motion Response of a Floating Wind-Wave Hybrid System. *J. Mar. Sci. Eng.* **2022**, *10*, 1660. [[CrossRef](#)]
49. Choi, K.; Yang, D.; Park, S.; Cho, B. Design and performance test of hydraulic PTO for wave energy converter. *Int. J. Precis. Eng. Manuf.* **2012**, *13*, 795–801. [[CrossRef](#)]
50. Gao, H.; Xiao, J. Effects of power take-off parameters and harvester shape on wave energy extraction and output of a hydraulic conversion system. *Appl. Energy* **2021**, *299*, 117278. [[CrossRef](#)]
51. Liu, C.; Hu, M.; Zhao, Z.; Zeng, Y.; Gao, W.; Chen, J.; Yan, H.; Zhang, J.; Yang, Q.; Bao, G. Latching control of a raft-type wave energy converter with a hydraulic power take-off system. *Ocean Eng.* **2021**, *236*, 109512. [[CrossRef](#)]
52. Xue, G.; Zhang, Z.; Qin, J.; Huang, S.; Liu, Y. Control Parameters Optimization of Accumulator in Hydraulic Power Take-Off System for Eccentric Rotating Wave Energy Converter. *J. Mar. Sci. Eng.* **2023**, *11*, 792. [[CrossRef](#)]
53. Zhang, N.; Zhang, X.; Xiao, L.; Wei, H.; Chen, W. Evaluation of long-term power capture performance of a bistable point absorber wave energy converter in South China Sea. *Ocean Eng.* **2021**, *237*, 109338. [[CrossRef](#)]
54. Newman, J.N. The exciting forces on fixed bodies in waves. *J. Ship Res.* **1962**, *6*, 10–17. [[CrossRef](#)]
55. Cummins, W.E. *The Impulse Response Function and Ship Motions*; David Taylor Model Basin: Washington, DC, USA, 1962.
56. Ogden, D.; Ruehl, K.; Yu, Y.; Keester, A.; Forbush, D.; Leon, J.; Tom, N. Review of WEC-Sim development and applications. *Int. Mar. Energy J.* **2022**, *5*, 5–9. [[CrossRef](#)]
57. Tampier, G.; Grueter, L. Hydrodynamic analysis of a heaving wave energy converter. *Int. J. Mar. Energy* **2017**, *19*, 304–318. [[CrossRef](#)]

Disclaimer/Publisher’s Note: The statements, opinions and data contained in all publications are solely those of the individual author(s) and contributor(s) and not of MDPI and/or the editor(s). MDPI and/or the editor(s) disclaim responsibility for any injury to people or property resulting from any ideas, methods, instructions or products referred to in the content.